Magnetic Resonance Materials in Physics, Biology and Medicine (2021) 34:581–591
https://doi.org/10.1007/s10334-021-00916-1

RESEARCH ARTICLE

EGFR-specific single-chain variable fragment antibody-conjugated Fe_3O_4/Au nanoparticles as an active MRI contrast agent for NSCLC

Yuan Lu[1] · Jing Huang[1] · Fakai Li[2] · Yuan Wang[3] · Ming Ding[1] · Jian Zhang[4] · Hong Yin[5] · Rui Zhang[6] · Xinling Ren[7]

Received: 9 December 2020 / Revised: 4 February 2021 / Accepted: 5 February 2021 / Published online: 24 February 2021

Abstract

Overexpression of epidermal growth factor receptor (EGFR) is closely associated with a poor prognosis in non-small cell lung cancer (NSCLC), thus making it a promising biomarker for NSCLC diagnosis. Here, we conjugated a single-chain antibody (scFv) targeting EGFR with Fe_3O_4/Au nanoparticles to form an EGFR-specific molecular MRI bioprobe (scFv@Fe_3O_4/Au) to better detect EGFR-positive NSCLC tumors in vivo. In vitro, we demonstrated that the EGFR-specific scFv could specifically deliver Fe_3O_4/Au to EGFR-positive NSCLC cells. In vivo experiments showed that the accumulation of scFv@Fe_3O_4/Au in tumor tissue was detectable by magnetic resonance imaging (MRI) at the indicated time points after systemic injection. The T2W signal-to-noise ratio (SNR) of EGFR-positive SPC-A1 tumors was significantly decreased after scFv@Fe_3O_4/Au injection, which was not observed in the tumors of mice injected with BSA@Fe_3O_4/Au. Furthermore, transmission electron microscopy (TEM) analysis showed the specific localization of scFv@Fe_3O_4/Au in the SPC-A1 tumor cell cytoplasm. Collectively, the results of our study demonstrated that scFv@Fe_3O_4/Au might be a useful probe for the noninvasive diagnosis of EGFP-positive NSCLC.

Keywords NSCLC · MRI · EGFR · Superparamagnetic iron oxide nanoparticle

Introduction

Lung cancer has the most rapidly increasing incidence rate worldwide, and 85% of all cases are non-small cell lung cancer (NSCLC) [1]. The majority of NSCLCs are often advanced at diagnosis, and the current 5-year survival rate is less than 15% [2, 3]. Although tyrosine kinase inhibitor (TKI)-targeted therapy and anti-PD-1/PD-L1 immunotherapy lead to better disease control, improved quality of life and prolonged progression-free survival (PFS) in subsets of patients, the outcome for more than 50% of patients remains suboptimal. These patients do not benefit from these novel therapies due to the absence of activating mutations or a lack of PD-1/PD-L1 expression [4]. Therefore, the accurate identification and timely resection of lung cancer at an early stage are critical for efficiently reducing cancer-related death. State-of-the-art imaging methods, such as low-dose computed tomography (CT), fluorine-18 fluorodeoxyglucose

✉ Hong Yin
yinhong@fmmu.edu.cn

✉ Rui Zhang
ruizhang@fmmu.edu.cn

✉ Xinling Ren
renxlmaj@126.com

[1] Department of Respiratory and Critical Care Medicine, Zhongda Hospital, Southeast University, Nanjing, Jiangsu, China

[2] Department of Respiratory and Critical Care Medicine, Jinhua Guangfu Hospital, Jinhua, Zhejiang, China

[3] The Second Section of Internal Medicine, Xi'an Thoracic Hospital, Xi'an, Shannxi, China

[4] Department of Respiratory and Critical Care Medicine, Xijing Hospital, Air Force Medical University of PLA (the Fourth Military Medical University), Xi'an, China

[5] Department of Radiology, Xijing Hospital, Air Force Medical University of PLA (the Fourth Military Medical University), Xi'an, Shannxi, China

[6] The State Key Laboratory of Cancer Biology, Department of Immunology, Air Force Medical University of PLA (the Fourth Military Medical University), Xi'an, Shannxi, China

[7] Department of Respiratory, Shenzhen University General Hospital, Shenzhen University, Xueyuan Ave. 1098, Shenzhen 518055, Guangdong, China

positron emission tomography (F18FDG-PET) and magnetic resonance imaging (MRI), have been widely utilized for the screening, diagnosis and staging of lung cancers in the clinic [5]. However, these techniques have their own disadvantages. LDCT identifies a relatively high percentage of benign nodules, and future repeat imaging that results in increased radiation exposure might be required [6]. F-18 FDG-PET has been widely used for differentiating benign from malignant lesions. However, false positive results can be produced by inflammation that has an abnormally increased uptake of FDG. In addition, malignant nodules smaller than 5 mm in diameter can cause false negative results [7].

MR imaging provides good anatomical details and might be a noninvasive diagnostic and staging tool for lung cancer [8]. Chest wall and mediastinal invasion, which is usually difficult to distinguish from the simple contiguity of tumors by CT scanning, could be effectively assessed based on superior soft-tissue contrast resolution of MRI [9]. Moreover, it is safe to use in sensitive patient groups (children, pregnant and lactating patients), because no ionizing radiation is utilized during the examination. However, limitations, such as a low proton density in the lung, a fast signal decay due to susceptibility artifacts at air-tissue interfaces, the relatively long time required for study acquisition, and a relatively low spatial resolution, have hampered its clinical application in the diagnosis of lung diseases [10–12]. Significant efforts have been made to design additional sequences to avoid the influence of breath and provide more information about pulmonary embolisms, tissue consolidation and pleural effusion [13]. Currently, the accuracy of MRI detection for lung nodules depends on the nodule size. The overall detection rates for nodules smaller than 10 mm in diameter ranged between 45 and 96% in different MRI sequences [14, 15]. Furthermore, microscopic invasion of lung cancers is hard to detect by current MRI technology. Developing novel diagnostic strategies for MRI is of clinical importance to improve the detection accuracy of lung cancers.

Molecular imaging methods, which employ lesion-specific bioprobes and engineered nanoparticles, have allowed the detection of small tumors by dramatically improving retention times and contrast [16, 17]. Bioprobes, namely, antibodies, single-chain fragment antibodies (scFvs), or small peptides, can recognize and bind to specific biomarkers such as antigens or receptors. Upon the process of binding, bioprobes could mediate internalization of the conjugated nanoparticles, which are tagged as imaging reporters for visualization [18]. Superparamagnetic iron oxide nanoparticles (SPIONs) are highly sensitive to MR detection[19]. Previous studies showed that the local concentration of SPIONs, as an imaging contrast agent in the tumor site, can be significantly increased after being conjugated with antibodies, scFvs and peptides. As a result, the imaging quality of many solid tumors, such as glioblastoma, breast cancers, lung cancers and prostate tumors, could be consequently improved [20–24].

Epidermal growth factor receptor (EGFR), a 170-kDa transmembrane protein, is composed of an extracellular ligand-binding domain, a single transmembrane domain, and an intracellular tyrosine kinase domain. By binding with ligands, EGFR regulates downstream signaling pathways and plays an important role in tumor cell proliferation, survival, migration, and metastasis. EGFR is overexpressed in over 60% of NSCLCs, which makes it the most important biomarker for lung cancer targeted therapy in recent decades [25]. Previously, we generated a fusion protein composed of an EGFR-targeting scFv and a nine-mer arginine peptide that can efficiently deliver siRNA into EGFR-positive NSCLC cells [26]. In the present study, we synthesized scFv@Fe_3O_4/Au by covalently conjugating EGFR-specific scFv with Fe_3O_4/Au nanoparticles. We analyzed the characterization of scFv@Fe_3O_4/Au and assessed its feasibility as an MRI agent for detecting lung cancer.

Materials and methods

Cell lines

The EGFR-positive lung cancer cell line SPC-A1 was obtained from Shanghai Institutes for Biological Sciences (Chinese Academy of Sciences, China), and the EGFR-deficient cell line H69 was obtained from Beijing Cell Resource Center (Chinese Academy of Medical Science, China). The two cell lines were all grown in RPMI-1640 culture medium supplemented with 10% fetal bovine serum (Gibco, Life Technologies, USA) at 37 °C under a mixture of 95% air and 5% CO_2.

scFv@Fe_3O_4/Au construction

EGFR-specific scFv was designed, generated and purified as previously described [26]. After purification, scFv was used for the construction of the MRI molecular bioprobe, and bovine serum albumin (BSA, Wilson, China) served as a control. The Fe_3O_4/Au nanoparticles used in this study were purchased from GoldMag Biotechnology Co., Ltd. (Xi'an, China), and the average diameter was 30 nm. Fe_3O_4/Au was functionalized by mixing with 1 mM aqueous L-cysteine hydrochloride (L-Cys) at room temperature for 12 h. One milligram of Fe_3O_4/Au (5 mg/ml) was dissolved in 50 mM MES buffer (pH 6.0) and then gently mixed together with 200 µl (5 mM) of 1-ethyl-3-(3-dimethylaminopropyl) carbodiimide (EDC) and 200 µl (10 mM) of NHS at room temperature for 15 min. After activating the reaction, Fe_3O_4/Au was covalently linked to 200 µg of scFv (1 mg/ml) or BSA (1 mg/ml) at room temperature to form scFv@Fe_3O_4/Au and

BSA@Fe_3O_4/Au. The solution buffer of scFv@Fe_3O_4/Au and BSA@Fe_3O_4/Au was exchanged into PBS (pH 7.4) by ultrafiltration, and unconjugated protein was also removed after the process. The conjugation efficiency of Fe_3O_4/Au was determined using a UV–visible spectrophotometer (PerkinElmer, MA, USA), and the conjugation efficiency (percentage of protein uptake) was calculated using equation: $(1-\frac{OD_{(post)}}{OD_{(pre)}})\times 100\%$. $OD_{(pre)}$ and $OD_{(post)}$ represent the absorbance at 280 nm of 50 µl of pre- and postconjugated solutions, respectively. The average size and zeta potential of scFv@Fe_3O_4/Au were evaluated using the electrophoretic mode of a Zetasizer Nano ZS (Malvern Instruments, UK). A transmission electron microscopy (TEM) system (JEM-1400, JEOL, Japan) was used to determine the shape and surface morphology of these nanoparticles. The conjugation was also analyzed by Coomassie-Blue SDS-PAGE.

In vitro assay of scFv@Fe_3O_4/Au internalization

Specific binding was first evaluated using laser scanning confocal microscopy (LSCM, A1, Nikon, Japan). For the LSCM assay, SPC-A1 and H69 cells were plated onto glass coverslips at 37 °C overnight. After adhering to the coverslips, the cells were incubated with 10 µg of scFv@Fe_3O_4/Au or BSA@Fe_3O_4/Au at 37 °C for 6 h, followed by incubation with an anti-His tag mouse antibody (Novagen, Merck Chemicals Ltd, USA) and a Cy3-labeled goat anti-mouse secondary antibody (Boster, Wuhan, China) for 1 h. The cells were then fixed in 4% (W/V) paraformaldehyde in PBS for 15 min, and nuclei were stained with 1.5 µg/ml 4,6-diamidino-2-phenylindole dihydrochloride (DAPI, Sigma-Aldrich, USA) at room temperature for 5 min. After washing in PBS, the intracellular distribution of bioprobes was visualized with LSCM. To visualize the internalization of Fe_3O_4/Au nanoparticles, some nanoparticles were prelabeled with coumarin-6 (RuixiBio, Xian, China) before conjugation.

For the FCM assay, 10 µg of scFv@Fe_3O_4/Au or BSA@Fe_3O_4/Au labeled with coumarin-6 was added to the culture medium of lung cancer cells at 37 °C for 6 h. Subsequently, the cells were incubated with anti-His tag mouse antibody at room temperature for 2 h, followed by incubation with FITC-labeled goat anti-mouse secondary antibody (Boster, Wuhan, China) at 4 °C for 1 h. After being washed once with ice-cold PBS, 10,000 cells were analyzed for fluorescence intensity using a FACSCalibur flow cytometer (FCM, BD Bioscience, Mountain View, CA) with Cell-Quest software (BD Bioscience).

When cells were grown to > 80% confluence, 10 µg of Fe_3O_4/Au, scFv@Fe_3O_4/Au, or BSA@Fe_3O_4/Au was added to the cell culture medium for 6 h. Cells were washed with PBS and then fixed with 4% glutaraldehyde before being analyzed by TEM.

In vivo assessment of scFv@Fe_3O_4/Au distribution

Nude mice (male Balb/c mice, weighing between 25 and 30 g, aged 4–6 weeks) were used for this study, which was conducted with the approval of the Institutional Animal Care and Use Committee of the Air Force Medical University of PLA (Xi'an, China) and conformed to institutional guidelines for the care and use of laboratory animals. For creation of the xenograft mouse model, 5×10^6 SPC-A1 or H69 cells were harvested, washed and resuspended in a low-temperature PBS/Matrigel (BD Biosciences, USA) mixture at a 1:1 ratio and injected into the thighs of nude mice. Two weeks after lung cancer cell injection, nude mice were randomized into the indicated groups of seven each. scFv, scFv@Fe_3O_4/Au and BSA@Fe_3O_4/Au were labeled with infra-red dye Dylight800 (Thermo Scientific, Rockford, USA) according to the manufacturer's specifications. Nude mice were injected with 0.1 µmol/kg DyLight800-labeled scFv, scFv@Fe_3O_4/Au and BSA@Fe_3O_4/Au. Eight hours after injection, fluorescence was imaged with a Xenogen IVIS Lumina II Imaging System (Caliper, PerkinElmer, USA). Identical illumination settings (ex: 745 nm/em: 840 nm, 2/f stop, 12.5 cm field of view, Binning factor of 4, 1 min exposure time) were used for all images. Fluorescence intensity was calculated using Living Image software and presented as photon flux (p/s/cm2/sr). To parallel the in vivo fluorescence living imaging (FLI), mice were then sacrificed, and tissues were isolated and homogenized for fluorescence quantification with a nanodrop2000 (Thermo Scientific, Rockford, USA). Tissue fluorescence was expressed as relative light units (RLU) per milligram of tissue. Tumor biopsies were also inspected by TEM.

MRI procedure

These studies were performed using a clinical 3.0 T whole-body MRI system (Siemens Magnetom Trio, Erlangen, Germany). The system is capable of operating at a maximum slew rate of 200 mT/m/ms and a maximum gradient strength of 40 mT/m. The tumor-bearing model was established as described above. The nude mice were anesthetized with 5% chloral hydrate at 0.2 ml per mouse via intraperitoneal injection. Once sedated, the mice were injected with 0.2 mg (in 0.2 ml of PBS) of scFv@Fe_3O_4/Au and BSA@Fe_3O_4/Au via the tail vein. T2-weighted (T2W) MRI scans were performed 4 h after injection. For each mouse, following localization scout scans, TSE T2W (repetition time/echo time = 3000/85 ms; slice thickness = 3 mm; field of view = 56.25×100 mm^2; slice thickness/slab thickness = 2/12.8 mm; matrix size = 72×128) measurements

were performed. Images were analyzed using ImageJ (version 2.1.4.7, NIH, MD, USA) as previously described [27]. Briefly, regions of interest were drawn encompassing cross sections of mouse tumors (regions of interest included approximately 40 voxels for each tumor) to measure the mean T2W signal intensity (S_{mean}). Regions of interest were chosen and analyzed to estimate the relative noise level. The relative signal-to-noise ratio (SNR) ($=S_{mean}/N_{SD}$) was calculated based upon the standard deviation of the background signal (N_{SD}).

Statistical methods

For both the in vitro and in vivo data, statistical analyses were performed with one-way ANOVA using SPSS 22.0. A p value of <0.05 was considered significant.

Results

Construction of immunonanoparticles

Previously, we constructed an EGFR-targeted scFv by sequentially fusing with the G4S linker, and the molecular weight was approximately 26 kDa [26]. In the present study, Fe_3O_4/Au nanoparticles functionalized with L-Cys were used to covalently bind with the scFv using NHS/EDC chemistry (Fig. 1a). The average diameter of scFv@Fe_3O_4/Au was 76.3 nm (sFig. 1A and B), which was nearly 50% larger than the unconjugated particles. The conjugation also resulted in a slight increase in the zeta potential, which increased from -24 to -28 mV.

SDS-PAGE was used to confirm the conjugation of scFv and Fe_3O_4/Au. ScFv migration was abolished after conjugation with Fe_3O_4/Au (Fig. 1b). We also performed western blotting to detect the Fe_3O_4/Au-conjugated scFv using an anti-His tag antibody. A positive stripe, as shown in sFig. 1C, proved that the EGFR-specific scFv bound to the surface of Fe_3O_4/Au nanoparticles. The conjugation efficiency gradually decreased with increasing concentrations of scFv or BSA (Fig. 1c). Specifically, adding 120 μg of scFv to 1 mg of Fe_3O_4/Au nanoparticles yielded a conjugation efficiency close to 95%. To avoid bias, conjugation efficiency was also determined for the control BSA. Under similar conditions, the conjugation efficiency between BSA and Fe_3O_4/Au was approximately 84%.

scFv@Fe_3O_4/Au retained the EGFR binding ability

scFv@Fe_3O_4/Au or BSA@Fe_3O_4/Au was added to the cell culture medium of EGFR-positive SPC-A1 and EGFR-deficient H69 cells for 6 h following incubation with an anti-His tag antibody and Cy3-labeled secondary antibody, after which the intracellular localization of scFv and scFv@Fe_3O_4/Au represented by a fluorescence signal was visualized by LSCM and quantified by FCM. SPC-A1 cells incubated with scFv@Fe_3O_4/Au showed bright red fluorescence (Fig. 2a). The signals of scFv alone and scFv@Fe_3O_4/Au were observed on cell membranes, dispersed in cytoplasms and even located in the nuclei of EGFR-positive cells. However, no red fluorescence was observed in SPC-A1 cells incubated with BSA or BSA@Fe_3O_4/Au. For H69 cells, no positive fluorescence signal was detected in any of the four groups. Similarly, SPC-A1 cells incubated with coumarin-6-labeled scFv@Fe_3O_4/Au or BSA@Fe_3O_4/Au showed positive intracellular green fluorescence. In the FCM assay, a shifted cellular FITC peak, which represents an increased number of Cy3- or coumarin-6-positive cells, was not observed in H69 cells but in SPC-A1 cells incubated with scFv@Fe_3O_4/Au (Fig. 2b). SPC-A1 cells incubated with BSA@Fe_3O_4/Au did not show a fluorescence shift as well.

TEM assays showed that SPC-A1 cells could effectively take up scFv@Fe_3O_4/Au nanoparticles, which were scattered in the cell cytoplasm (Fig. 2c). However, no intracellular aggregates of nanoparticles were observed in cells incubated with BSA@Fe_3O_4/Au. In addition, no nanoparticles were found in the cytoplasm of EGFR-deficient H69 cells, which further confirmed the specific binding and internalization ability of scFv@Fe_3O_4/Au.

In vivo EGFR-targeted nanoparticles delivery

The in vivo distribution of DyLight 800-labeled scFv and scFv@Fe_3O_4/Au was examined in nude mouse models using a whole-body near-infrared FLI system. The model was established by subcutaneous injection of SPC-A1 and H69 cells. After xenografts grew locally around the injection site, we injected DyLight 800-labeled scFv, scFv@Fe_3O_4/Au or BSA@Fe_3O_4/Au via the mouse tail vein. As shown by the FLI panel, 8 h later, scFv and scFv@Fe_3O_4/Au were gradually removed from normal tissues and enriched in the tumors (Fig. 3a). In contrast, BSA@Fe_3O_4/Au was removed from the body, and fluorescence was detected mainly in kidneys rather than in tumors. In this study, the strongest fluorescence uptake in tumors quantified by the relative fluorescence intensity of homogenate occurred in the groups treated with scFv and scFv@Fe_3O_4/Au compared to relatively weak signals detected in kidneys and liver and negligible accumulation in heart, lung and muscle (Fig. 3b). To assess the intracorporeal scFv-mediated nanoparticle distribution, sectional slices of the tumors were examined under a TEM system. Fe_3O_4/Au was deposited in SPC-A1 xenograft cells treated with scFv@Fe_3O_4/Au but not in cells treated with scFv or BSA@Fe_3O_4/Au (Fig. 3c). H69 xenograft cells were incapable of taking up nanoparticles.

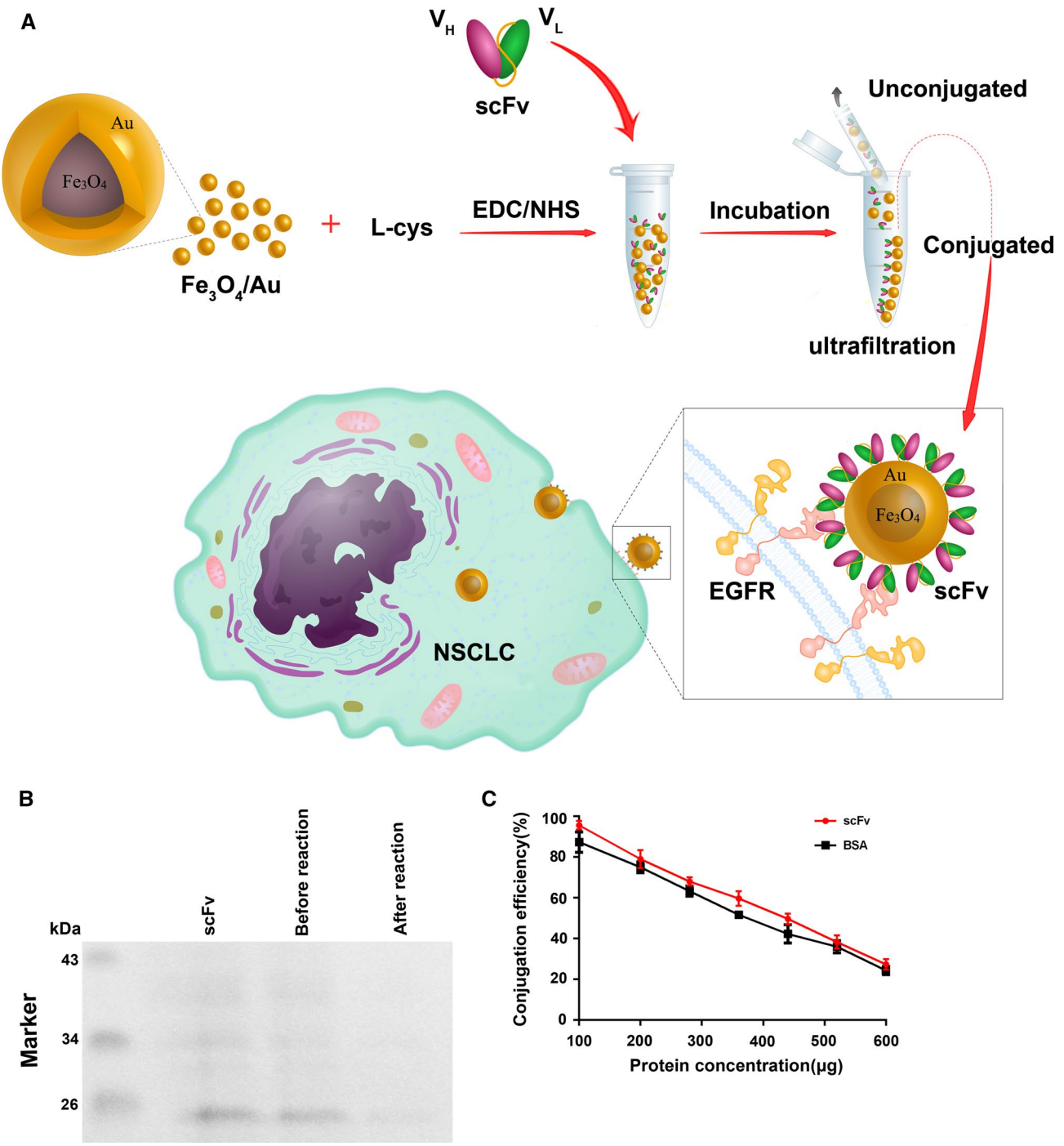

Fig. 1 **a** Schematic illumination of EGFR-specific scFv@Fe_3O_4/Au construction and internalization in NSCLC cells. **b** Assessment of scFv conjugation to the surface of Fe_3O_4/Au through a covalent linkage by SDS-PAGE. **c** Coupling efficiency assay of scFv@Fe_3O_4/Au

In vivo MRI detection of EGFR-positive tumors by scFv@Fe_3O_4/Au

To evaluate the feasibility of using the immunonanoparticles as an MRI contrast agent, we injected lung cancer xenograft mice with BSA@Fe_3O_4/Au and scFv@Fe_3O_4/Au via the tail vein. Four hours later, a clear signal intensity change was observed in SPC-A1 tumors (Fig. 4). After MR images of the tumor were obtained, we calculated the SNR pre- and postimaging. The T2W SNR of tumors in SPC-A1 xenograft mice injected with scFv@Fe_3O_4/Au demonstrated a significant decrease after injection (172.1 ± 7.73 vs

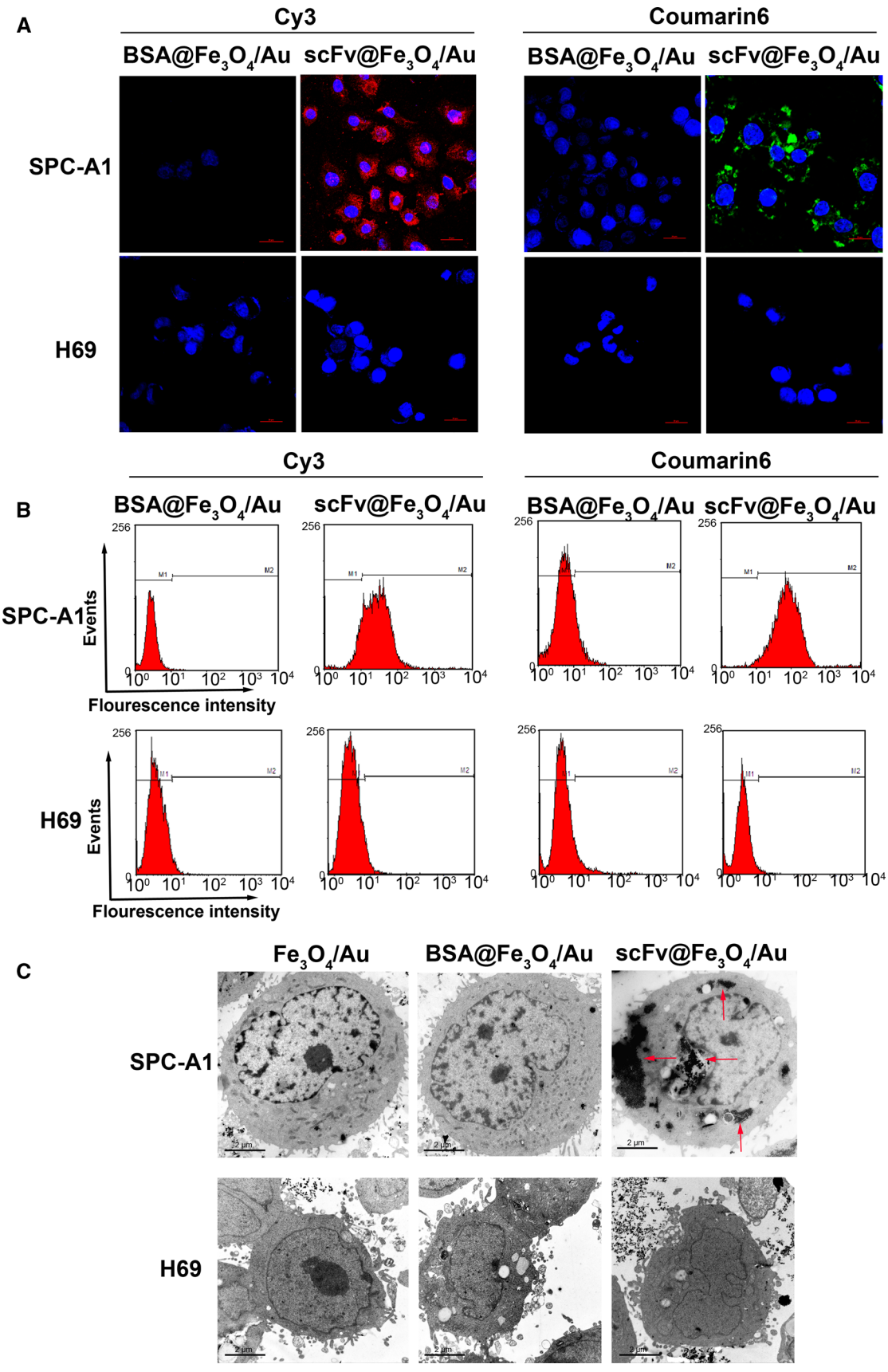
A
Cy3
Coumarin6
BSA@Fe3O4/Au
scFv@Fe3O4/Au
BSA@Fe3O4/Au
scFv@Fe3O4/Au
SPC-A1
H69
B
Cy3
Coumarin6
BSA@Fe3O4/Au
scFv@Fe3O4/Au
BSA@Fe3O4/Au
scFv@Fe3O4/Au
SPC-A1
H69
Events
Flourescence intensity
C
Fe3O4/Au
BSA@Fe3O4/Au
scFv@Fe3O4/Au
SPC-A1
H69

◂**Fig. 2** **a** Internalization of scFv and scFv@Fe_3O_4/Au was visualized by LSCM (DAPI, *blue*; Cy3, *red*; Coumarin-6, *green*), Scale bar = 20 μm. **b** Binding to EGFR-positive NSCLC cells was assessed by FCM. **c** Intercellular location of Fe_3O_4/Au (punctate black spots pointed by *red arrows*) in TEM images of lung cancer cells (12,000×)

90.73 ± 7.39, $p = 0.002$) (sFig. 2A and sTable 1). However, there was no obvious change in the tumor SNR from SPC-A1 xenograft mice that received BSA@Fe_3O_4/Au injection (178.60 ± 14.32 vs 168.80 ± 14.63, $p = 0.659$). Meanwhile, the liver and spleen from the same mice exhibited a significant SNR decrease 4 h after injection of either scFv@Fe_3O_4/Au or BSA@Fe_3O_4/Au. Meanwhile, a mild but not statistically significant SNR change was detected in the kidney at the same time point after injection.

For H69 xenograft mice, neither BSA@Fe_3O_4/Au nor scFv@Fe_3O_4/Au injection evoked a signal intensity change in tumors. There was no statistically significant T2W SNR decrease (176.7 ± 5.68 vs 170.5 ± 5.07, $p = 0.458$; 167.4 ± 6.13 vs 165.2 ± 5.97, $p = 0.809$, respectively). The liver and spleen exhibited marked changes in SNR at 4 h after the injection of scFv@Fe_3O_4/Au or BSA@Fe_3O_4/Au in comparison with tumor tissues (sFig. 2B and sTable 2). These results provide reliable receptor binding/internalization evidence and demonstrate that scFv@Fe_3O_4/Au has desirable specificity for the detection of NSCLC tumors in vivo.

Discussion

Contrast agents such as surface-engineered nanoparticles can greatly enhance the signal detection capability of MRI and thereby improve the detection rate of diseases in their early stages [28]. A gold shell of Fe_3O_4/Au can prevent the aggregation of nanoparticles, afford water solubility and improve biocompatibility[29]. Fe_3O_4/Au can be magnetized and become responsive by exposure to an external magnetic field [27].

There are two reasons for the popularity of nanoparticles in cancer studies: their high surface/volume ratio allows them to bind, absorb or carry other materials, such as small molecule drugs and probes, and their nanosized diameter (less than 100 nm) facilitates the process of cell internalization of antitumor agents [30, 31]. However, tumor-specific nanoparticle delivery is still a challenge from a clinical perspective. Nanoparticles are more prone to be deposited in the liver than in lesions [32]. Therefore, many studies have focused on improving the effectiveness of tumor targeting. Biomolecules, such as antibodies, peptides, and small molecules, have been bound on the surface of nanoparticles to provide efficient and targeted delivery of diagnostic or therapeutic reagents [33].

Overexpression of EGFR provides an ideal tumor biomarker in NSCLC patients and a basis for antibody-based tumor-targeting therapies. Several neutralizing antibodies have been studied preclinically or approved for inhibiting the EGFR signaling axis in NSCLC [34–37]. EGFR-specific antibodies or antibody fragments have been conjugated with gold nanoparticles in previous studies on squamous and urothelial cancer to provide superior lesion-targeting ability [38, 39]. The scFv consisting of tandemly connected variable domains (V_H and V_L) of the original antibody was an ideal tool for drug delivery, as the size was much smaller than the intact antibody due to lack of both the constant regions and the Fc domain, which means stronger penetrating capability and lower immunogenicity [40]. ScFv derivatives could specifically deliver synthetic materials and release them in the cytoplasm of targeted cells through the formation and internalization of antibody-antigen complexes [41]. Previously, we efficiently silenced the expression of targeted genes by utilizing EGFR-specific scFv as an siRNA carrier, which successfully restored the sensitivity of NSCLC cells to TKIs both in vitro and in vivo [26]. Another preclinical study also yielded promising results in which SPIONs conjugated with anti-EGFRvIII antibodies, a cancer-associated variant of EGFR, dramatically reduced the T2 value and enhanced MRI contrast of glioma xenografts in a nude mouse model [42].

Immobilization of scFv to Fe_3O_4/Au required covalent interactions, which did not compromise antigen recognition and cellular uptake of scFv. The intracellular localization of scFv and scFv@Fe_3O_4/Au represented by the fluorescence signal could be observed with LSCM and quantified by FCM. Moreover, Fe_3O_4/Au nanoparticles were increasingly deposited in the cytoplasm of EGFR-positive SPC-A1 cells but not in EGFR-deficient H69 cells through covalent coupling with scFv, as recorded by TEM images of in vitro or in vivo specimens.

The in vivo distribution of the SPIO-based bioprobe throughout the body was revealed by FLI and MRI assays, and the probe was gradually enriched in EGFR-positive SPC-A1 tumors but not in EGFR-negative H69 tumors. After passing through the tumor blood vessels, scFv@Fe_3O_4/Au entered the interior of the tumor cell through receptor-mediated endocytosis. The irrelevant protein BSA-conjugated Fe_3O_4/Au may enter the intercellular substance of tumors due to abnormalities in tumor blood vessels, but it could not trigger receptor-mediated endocytosis and thereby abundantly accumulated in targeted cells. There were two ways for the clearance of scFv@Fe_3O_4/Au from the body: most was excreted by the kidneys, and a minor amount gradually accumulated in the liver and spleen to enter iron metabolism [27]. In this study, relatively weak signals were

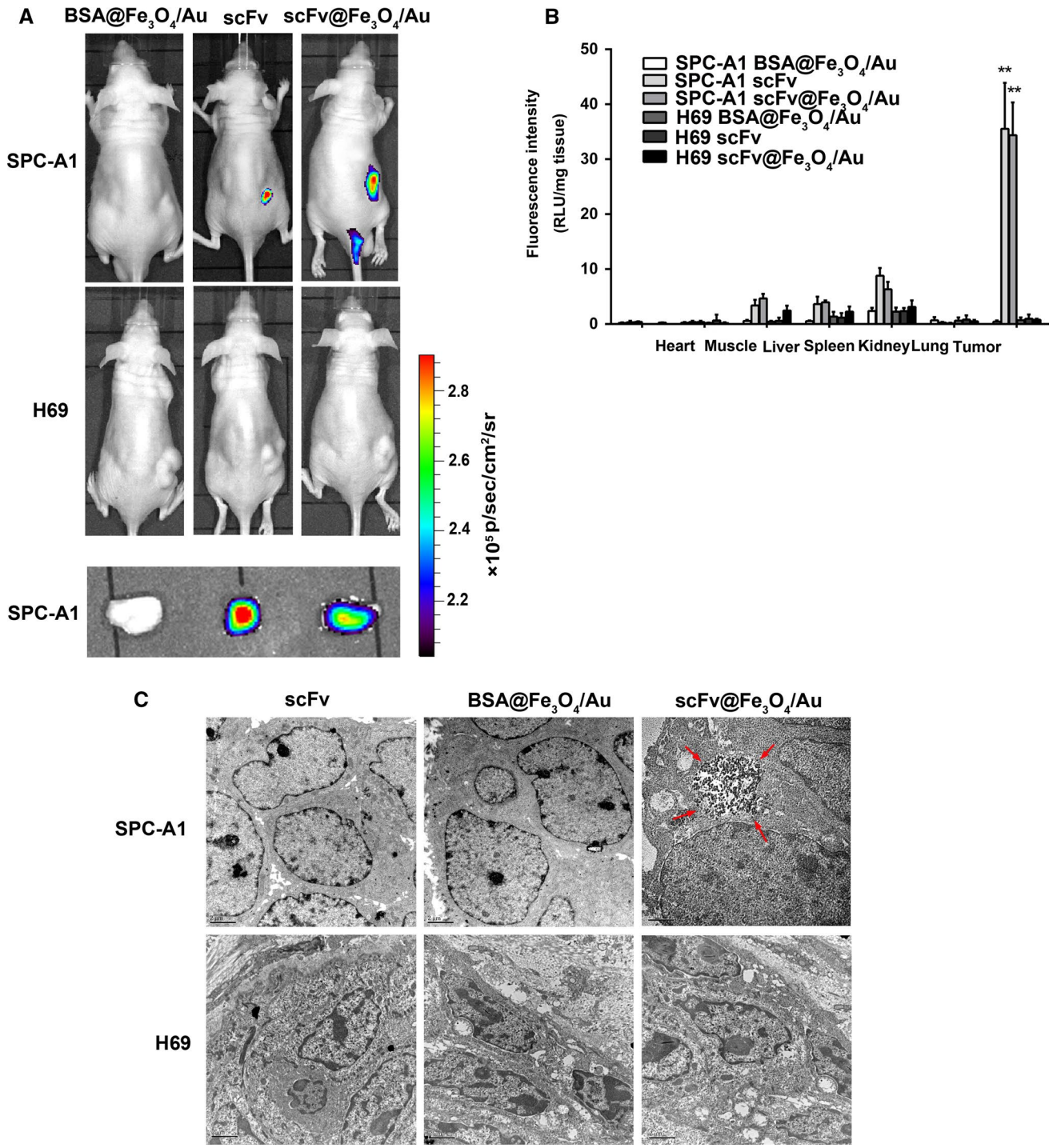

Fig. 3 **a** In vivo distribution of the DyLight 800-conjugated scFv, scFv@Fe_3O_4/Au and BSA@Fe_3O_4/Au 8 h after injection. **b** Fluorescence quantification of mice tissues. Data is expressed as relative light units (RLU) per mg tissue. $^{**}p < 0.01$. **c** Location of Fe_3O_4/Au (pointed by *red arrows*) in TEM images of tumor specimens (12,000×)

detected in the kidneys and liver; the fluorescence accumulation in the heart, lung and muscle was negligible. For H69 xenograft mice, no significant change in the T2W SNR was observed. These findings suggest that scFv@Fe_3O_4/Au might be a potential in vivo bioprobe in MR imaging with greater lesion-to-background contrast due to improved biodistribution, which was consistent with previous results [24].

There was discordance between the results from the FLI assay and the MRI scan. In the FLI assay, the kidney had the next strongest fluorescence intensity behind the tumor

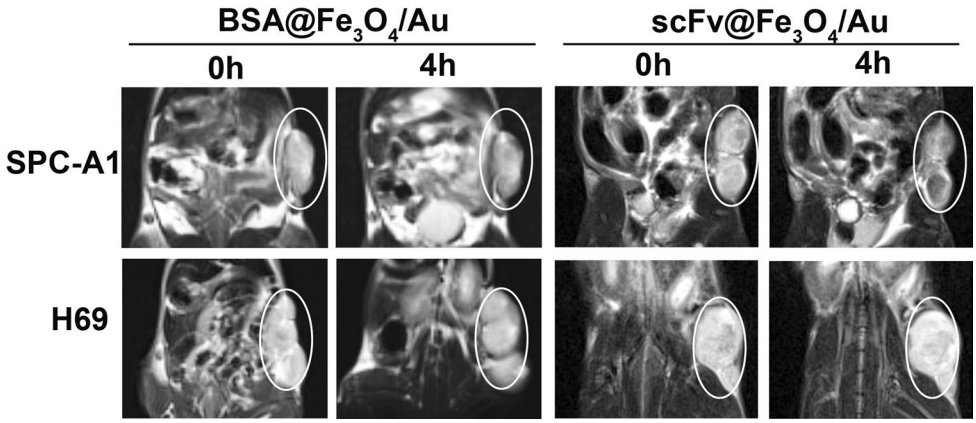

Fig. 4 T2W signal intensity change of mice xenografts was detected by in vivo MRI imaging

tissue. However, the signal intensity change of the kidney in the MRI scan was negligible. This result may have been due to the different metabolic mechanisms of scFv and nanoparticles. ScFv was mainly eliminated from the body through the kidney, while nanoparticles were cleaned by phagocytic cells in the reticuloendothelial system [43]. Further studies are necessary to investigate and clarify this phenomenon. Besides, the reasons for us to demonstrated the efficacy of scFv@Fe_3O_4/Au using the flank-implanted xenograft model rather than the lung are as follows: It's difficult for lung cancer cell line, especially H69, to form solid tumor in nude mice. We failed several times to form lesions in mice lungs. Since this study is the first step for using our scFv in MR imaging, we decided to move on with this model. We considered the data including those of control groups was proper enough to show the efficacy of our strategy. Importantly, we have no access to the labs in university to carry out further experiments, which are not open to hospital staffs according to anti-contagion policies of the COVID-19 pandemic.

Conclusion

Injection of intravenous contrast material in a primary MRI screening setting can effectively promote vascularization and increase enhancement. In this study, we used EGFR-specific scFv-modified Fe_3O_4/Au nanoparticles as a targeting MRI contrast agent. In vitro, EGFR-positive tumor cells exhibited substantial uptake of scFv@Fe_3O_4/Au. In vivo, the T2W SNR MRI signal in EGFR-positive tumors was significantly decreased after the injection of scFv@Fe_3O_4/Au. We believe that this work will provide a new strategy for the application of Fe_3O_4/Au nanoparticles and improve the accuracy of NSCLC diagnosis. Although there were no obvious acute toxicities observed during the in vivo experiments, further studies are certainly necessary to fully elucidate the safety of this bioprobe. The immune response caused by exogenous metal and artificial scFv should be taken into consideration and thoroughly evaluated [44, 45].

Supplementary Information The online version contains supplementary material available at https://doi.org/10.1007/s10334-021-00916-1.

Acknowledgements This study was funded by Jiangsu basic research program (Natural Science Foundation, No. BK20201484), National Natural Science Foundation of China (No. 81871880) and Jiangsu science and technology development project (No. BE2017745).

Author contributions Study conception and design: YL, HY, RZ, XLR. Acquisition of data: YL, YW. Analysis and interpretation of data: YL, FKL, HY, RZ, XLR. Drafting of manuscript: YL, RZ, XLR. Critical revision: MD, HY, RZ, XLR.

Compliance with ethical standards

Conflict of interest The authors declare that they have no conflicts of interest.

Ethical standards All in vivo was approved by the Institutional Animal Care and Use Committee of the Air Force Medical University of PLA (Approval number: AFMUIACU-201811-224-01).

Informed consent For this type of study, formal consent is not required.

References

1. Bray F, Ferlay J, Soerjomataram I, Siegel RL, Torre LA, Jemal A (2018) Global cancer statistics 2018: GLOBOCAN estimates of incidence and mortality worldwide for 36 cancers in 185 countries. CA Cancer J Clin 68(6):394–424
2. Manser R, Lethaby A, Irving LB, Stone C, Byrnes G, Abramson MJ, Campbell D (2013) Screening for lung cancer. Cochrane Database Syst Rev 21(6)
3. Hirsch FR, Scagliotti GV, Mulshine JL, Kwon R, Curran WJ Jr, Wu Y-L, Paz-Ares L (2017) Lung cancer: current therapies and new targeted treatments. Lancet 389(10066):299–311
4. Tessari A, Parbhoo K, Pawlikowski M, Fassan M, Rulli E, Foray C, Fabbri A, Embrione V, Ganzinelli M, Capece M (2018) RANBP9 affects cancer cells response to genotoxic stress and its

overexpression is associated with worse response to platinum in NSCLC patients. Oncogene 37(50):6463–6476
5. Vlahos I, Stefanidis K, Sheard S, Nair A, Sayer C, Moser J (2018) Lung cancer screening: nodule identification and characterization. Transl Lung Cancer Res 7(3):288
6. Bach PB, Mirkin JN, Oliver TK, Azzoli CG, Berry DA, Brawley OW, Byers T, Colditz GA, Gould MK, Jett JR, Sabichi AL, Smith-Bindman R, Wood DE, Qaseem A, Detterbeck FC (2012) Benefits and harms of CT screening for lung cancer: a systematic review. JAMA J Am Med Assoc 307(22):2418–2429
7. Treglia G, Sadeghi R, Annunziata S, Lococo F, Cafarotti S, Prior JO, Bertagna F, Ceriani L, Giovanella L (2014) Diagnostic performance of fluorine-18-fluorodeoxyglucose positron emission tomography in the assessment of pleural abnormalities in cancer patients: a systematic review and a meta-analysis. Lung Cancer 83(1):1–7
8. Lee WK, Lau EW, Chin K, Sedlaczek O, Steinke K (2013) Modern diagnostic and therapeutic interventional radiology in lung cancer. J Thor Dis 5(Suppl 5):S511–S523
9. Biederer J, Hintze C, Fabel M (2008) MRI of pulmonary nodules: technique and diagnostic value. Cancer Imaging 8:125–130
10. Wielputz MO, Heussel CP, Herth FJ, Kauczor HU (2014) Radiological diagnosis in lung disease: factoring treatment options into the choice of diagnostic modality. Dtsch Arztebl Int 111(11):181–187
11. Islam S, Walker RC (2013) Advanced imaging (positron emission tomography and magnetic resonance imaging) and image-guided biopsy in initial staging and monitoring of therapy of lung cancer. Cancer J 19:208–216
12. Puderbach M, Hintze C, Ley S, Eichinger M, Kauczor HU, Biederer J (2007) MR imaging of the chest: a practical approach at 1.5T. Eur J Radiol 64(3):345–355
13. Kim HS, Lee KS, Ohno Y, van Beek EJ, Biederer J (2015) PET/CT versus MRI for diagnosis, staging, and follow-up of lung cancer. J Magn Reson Imaging 42(2):247–260
14. Koyama H, Ohno Y, Seki S, Nishio M, Yoshikawa T, Matsumoto S, Sugimura K (2013) Magnetic resonance imaging for lung cancer. J Thorac Imaging 28(3):138–150
15. Biederer J, Ohno Y, Hatabu H, Schiebler ML, van Beek EJR, Vogel-Claussen J, Kauczor HU (2017) Screening for lung cancer: does MRI have a role? Eur J Radiol 86:353–360
16. Xia Y, Xu C, Zhang X, Ning P, Wang Z, Tian J, Chen X (2019) Liposome-based probes for molecular imaging: from basic research to the bedside. Nanoscale 11(13):5822–5838
17. Laws MT, Bonomi RE, Kamal S, Gelovani DJ, Llaniguez J, Potukutchi S, Lu X, Mangner T, Gelovani JG (2019) Molecular imaging HDACs class IIa expression-activity and pharmacologic inhibition in intracerebral glioma models in rats using PET/CT/(MRI) with [18 F] TFAHA. Sci Rep 9(1):1–11
18. Montesi SB, Désogère P, Fuchs BC, Caravan P (2019) Molecular imaging of fibrosis: recent advances and future directions. J Clin Investig 129(1):24–33
19. Thakor AS, Gambhir SS (2013) Nanooncology: the future of cancer diagnosis and therapy. CA Cancer J Clin 63(6):395–418
20. Adolphi NL, Butler KS, Lovato DM, Tessier TE, Trujillo JE, Hathaway HJ, Fegan DL, Monson TC, Stevens TE, Huber DL, Ramu J, Milne ML, Altobelli SA, Bryant HC, Larson RS, Flynn ER (2012) Imaging of Her2-targeted magnetic nanoparticles for breast cancer detection: comparison of SQUID-detected magnetic relaxometry and MRI. Contrast Media Mol Imaging 7(3):308–319
21. Wang H, Zheng L, Peng C, Shen M, Shi X, Zhang G (2013) Folic acid-modified dendrimer-entrapped gold nanoparticles as nanoprobes for targeted CT imaging of human lung adencarcinoma. Biomaterials 34(2):470–480
22. Chen F, Ma K, Madajewski B, Zhuang L, Zhang L, Rickert K, Marelli M, Yoo B, Turker MZ, Overholtzer M (2018) Ultrasmall targeted nanoparticles with engineered antibody fragments for imaging detection of HER2-overexpressing breast cancer. Nat Commun 9(1):1–11
23. Yeh C-Y, Hsiao J-K, Wang Y-P, Lan C-H, Wu H-C (2016) Peptide-conjugated nanoparticles for targeted imaging and therapy of prostate cancer. Biomaterials 99:1–15
24. Wang Z, Qiao R, Tang N, Lu Z, Wang H, Zhang Z, Xue X, Huang Z, Zhang S, Zhang G (2017) Active targeting theranostic iron oxide nanoparticles for MRI and magnetic resonance-guided focused ultrasound ablation of lung cancer. Biomaterials 127:25–35
25. Nicholson RI, Gee JM, Harper ME (2001) EGFR and cancer prognosis. Eur J Cancer 37(4):S9-15
26. Lu Y, Liu L, Wang Y, Li F, Zhang J, Ye M, Zhao H, Zhang X, Zhang M, Zhao J, Yan B, Yang A, Feng H, Zhang R, Ren X (2016) siRNA delivered by EGFR-specific scFv sensitizes EGFR-TKI-resistant human lung cancer cells. Biomaterials 76:196–207
27. Ren J, Zhang Z, Wang F, Yang Y, Liu Y, Wei G, Yang A, Zhang R, Huan Y, Cui Y, Larson AC (2012) MRI of prostate stem cell antigen expression in prostate tumors. Nanomedicine (Lond) 7(5):691–703
28. Srinivasarao M, Galliford CV, Low PS (2015) Principles in the design of ligand-targeted cancer therapeutics and imaging agents. Nat Rev Drug Discovery 14(3):203–219
29. Farahavar G, Abolmaali SS, Gholijani N, Nejatollahi F (2019) Antibody-guided nanomedicines as novel breakthrough therapeutic, diagnostic and theranostic tools. Biomater Sci 7(10):4000–4016
30. Pasquetto MV, Vecchia L, Covini D, Digilio R, Scotti C (2011) Targeted drug delivery using immunoconjugates: principles and applications. J Immunother 34:611–628
31. Annapragada A (2015) Advances in nanoparticle imaging technology for vascular pathologies. Annu Rev Med 66(1):177–193
32. Nune SK, Gunda P, Thallapally PK, Lin YY, Forrest ML, Berkland CJ (2009) Nanoparticles for biomedical imaging. Exp Opin Drug Deliv 6(11):1175–1194
33. Greene M, Richards D, Nogueira J, Campbell K, Smyth P, Fernández M, Scott CJ, Chudasama V (2018) Forming next-generation antibody-nanoparticle conjugates through the oriented installation of non-engineered antibody fragments. Chem Sci 9(1):79–87
34. Pirker R, Pereira JR, von Pawel J, Krzakowski M, Ramlau R, Park K, de Marinis F, Eberhardt WEE, Paz-Ares L, Störkel S, Schumacher K-M, von Heydebreck A, Celik I, O'Byrne KJ (2012) EGFR expression as a predictor of survival for first-line chemotherapy plus cetuximab in patients with advanced non-small-cell lung cancer: analysis of data from the phase 3 FLEX study. Lancet Oncol 13:33–42
35. Freeman D (2009) Safety and efficacy of panitumumab in the treatment of metastatic colorectal cancer. Clin Med Therap 1:633–645
36. Harding J, Burtness B (2005) Cetuximab an epidermal growth factor receptor chimeric human-murine monoclonal antibody. Drugs Today 41(2):107–127
37. Talavera A, Friemann R, Gomez-Puerta S, Martinez-Fleites C, Garrido G, Rabasa A, Lopez-Requena A, Pupo A, Johansen RF, Sanchez O, Krengel U, Moreno E (2009) Nimotuzumab, an antitumor antibody that targets the epidermal growth factor receptor, blocks ligand binding while permitting the active receptor conformation. Cancer Res 69(14):5851–5859
38. Chen CH, Wu YJ, Chen JJ (2016) Photo-thermal therapy of bladder cancer with Anti-EGFR antibody conjugated gold nanoparticles. Frontiers Biosci (Landmark edn) 21:1211–1221
39. Manivasagan P, Nguyen VT, Jun SW, Hoang G, Mondal S, Kim H, Doan VHM, Kim J, Kim CS, Oh J (2019) Anti-EGFR antibody conjugated thiol chitosan-layered gold nanoshells for dual-modal

imaging-guided cancer combination therapy. J Control Rel 311–312:26–42
40. Lu Y, Wang Y, Zhang M, Liu L, Li F, Zhang J, Ye M, Zhao H, Zhao J, Yan B, Yang A, Zhang R, Li X, Ren X (2016) HER2-siRNA delivered by EGFR-specific single chain antibody inhibits NSCLC cell proliferation and tumor growth. Oncotarget 7(17):23594–23607
41. Friedlander E, Barok M, Szollosi J, Vereb G (2008) ErbB-directed immunotherapy: antibodies in current practice and promising new agents. Immunol Lett 116(2):126–140
42. Hadjipanayis CG, Machaidze R, Kaluzova M, Wang L, Schuette AJ, Chen H, Wu X, Mao H (2010) EGFRvIII antibody-conjugated iron oxide nanoparticles for magnetic resonance imaging-guided convection-enhanced delivery and targeted therapy of glioblastoma. Cancer Res 70(15):6303–6312
43. Bulte JW, Kraitchman DL (2004) Iron oxide MR contrast agents for molecular and cellular imaging. NMR Biomed 17(7):484–499
44. Lanone S, Boczkowski J (2006) Biomedical applications and potential health risks of nanomaterials: molecular mechanisms. Curr Mol Med 6(6):651–663
45. Zolnik BS, Gonzalez-Fernandez A, Sadrieh N, Dobrovolskaia MA (2010) Nanoparticles and the immune system. Endocrinology 151(2):458–465